Parameter constraints for flat cosmologies from cosmic microwave background and 2dFGRS power spectra

Will J. Percival,[1]* Will Sutherland,[1] John A. Peacock,[1] Carlton M. Baugh,[2] Joss Bland-Hawthorn,[3] Terry Bridges,[3] Russell Cannon,[3] Shaun Cole,[2] Matthew Colless,[4] Chris Collins,[5] Warrick Couch,[6] Gavin Dalton,[7,8] Roberto De Propris,[6] Simon P. Driver,[9] George Efstathiou,[10] Richard S. Ellis,[11] Carlos S. Frenk,[2] Karl Glazebrook,[12] Carole Jackson,[4] Ofer Lahav,[10] Ian Lewis,[3] Stuart Lumsden,[13] Steve Maddox,[14] Stephen Moody,[9] Peder Norberg,[2] Bruce A. Peterson[4] and Keith Taylor[3] (The 2dFGRS Team)

[1]*Institute for Astronomy, University of Edinburgh, Royal Observatory, Blackford Hill, Edinburgh EH9 3HJ*
[2]*Department of Physics, University of Durham, South Road, Durham DH1 3LE*
[3]*Anglo-Australian Observatory, PO Box 296, Epping, NSW 2121, Australia*
[4]*Research School of Astronomy & Astrophysics, The Australian National University, Weston Creek, ACT 2611, Australia*
[5]*Astrophysics Research Institute, Liverpool John Moores University, 12 Quays House, Birkenhead L14 1LD*
[6]*Department of Astrophysics, University of New South Wales, Sydney, NSW 2052, Australia*
[7]*Department of Physics, University of Oxford, Keble Road, Oxford OX1 3RH*
[8]*Space Science and Technology Division, Rutherford Appleton Laboratory, Chilton, Didcot OX11 0QX*
[9]*School of Physics and Astronomy, University of St Andrews, North Haugh, St Andrews, Fife KY6 9SS*
[10]*Institute of Astronomy, University of Cambridge, Madingley Road, Cambridge CB3 0HA*
[11]*Department of Astronomy, Caltech, Pasadena, CA 91125, USA*
[12]*Department of Physics & Astronomy, Johns Hopkins University, Baltimore, MD 21218-2686, USA*
[13]*Department of Physics, University of Leeds, Woodhouse Lane, Leeds LS2 9JT*
[14]*School of Physics & Astronomy, University of Nottingham, Nottingham NG7 2RD*

ABSTRACT

We constrain flat cosmological models with a joint likelihood analysis of a new compilation of data from the cosmic microwave background (CMB) and from the 2dF Galaxy Redshift Survey (2dFGRS). Fitting the CMB alone yields a known degeneracy between the Hubble constant h and the matter density Ω_m, which arises mainly from preserving the location of the peaks in the angular power spectrum. This 'horizon-angle degeneracy' is considered in some detail and is shown to follow the simple relation $\Omega_m h^{3.4} = $ constant. Adding the 2dF-GRS power spectrum constrains $\Omega_m h$ and breaks the degeneracy. If tensor anisotropies are assumed to be negligible, we obtain values for the Hubble constant of $h = 0.665 \pm 0.047$, the matter density $\Omega_m = 0.313 \pm 0.055$, and the physical cold dark matter and baryon densities $\Omega_c h^2 = 0.115 \pm 0.009$, $\Omega_b h^2 = 0.022 \pm 0.002$ (standard rms errors). Including a possible tensor component causes very little change to these figures; we set an upper limit to the tensor-to-scalar ratio of $r < 0.7$ at a 95 per cent confidence level. We then show how these data can be used to constrain the equation of state of the vacuum, and find $w < -0.52$ at 95 per cent confidence. The preferred cosmological model is thus very well specified, and we discuss the precision with which future CMB data can be predicted, given the model assumptions. The 2dFGRS power-spectrum data and covariance matrix, and the CMB data compilation used here, are available from http://www.roe.ac.uk/~wjp/.

Key words: cosmic microwave background – cosmological parameters – large-scale structure of Universe.

*E-mail: wjp@roe.ac.uk

1 INTRODUCTION

The 2dF Galaxy Redshift Survey (2dFGRS; see, e.g., Colless et al. 2001) has mapped the local Universe in detail. If the galaxy distribution has Gaussian statistics and the bias factor is independent of scale, then the galaxy power spectrum should contain all of the available information concerning the seed perturbations of cosmological structure: it is statistically complete in the linear regime. The power spectrum of the data as of early 2001 was presented in Percival et al. (2001), and was shown to be consistent with recent cosmic microwave background (CMB) and nucleosynthesis results.

In Efstathiou et al. (2002) we combined the 2dFGRS power spectrum with recent CMB data sets in order to constrain the cosmological model (see also subsequent work by Lewis & Bridle 2002). Considering a wide range of possible assumptions, we were able to show that the Universe must be nearly flat, requiring a non-zero cosmological constant Λ. The flatness constraint was quite precise ($|1 - \Omega_{tot}| < 0.05$ at 95 per cent confidence); since inflation models usually predict near-exact flatness ($|1 - \Omega_{tot}| < 0.001$; e.g. Section 8.3 of Kolb & Turner 1990), there is strong empirical and theoretical motivation for considering only the class of exactly flat cosmological models. The question of which flat universes match the data is thus an important one to be able to answer. Removing spatial curvature as a degree of freedom also has the practical advantage that the space of cosmological models can be explored in much greater detail. Therefore, throughout this work we assume a universe with baryons, cold dark matter (CDM) and vacuum energy summing to $\Omega_{tot} = 1$ (cf. Peebles 1984; Efstathiou, Sutherland & Maddox 1990).

In this work we also assume that the initial fluctuations were adiabatic, Gaussian and well described by power-law spectra. We consider models with and without a tensor component, which is allowed to have slope and amplitude independent of the scalar component. Recent Sudbury Neutrino Observatory (SNO) measurements (Ahmad et al. 2002) are most naturally interpreted in terms of three neutrinos of cosmologically negligible mass ($\lesssim 0.05$ eV, as opposed to current cosmological limits of the order of 2 eV – see Elgaroy et al. 2002). We therefore assume zero neutrino mass in this analysis. In most cases, we assume the vacuum energy to be a 'pure' cosmological constant with equation of state $w \equiv p/\rho c^2 = -1$, except in Section 5 where we explore $w > -1$.

In Section 2 we use a compilation of recent CMB observations (including data from VSA, Scott et al. 2002, and CBI, Pearson et al. 2002, experiments) to determine the maximum-likelihood amplitude of the CMB angular power spectrum on a convenient grid, taking into account calibration and beam uncertainties where appropriate. This compression of the data is designed to speed the analysis presented here, but it should be of interest to the community in general.

In Section 3 we fit to both the CMB data alone, and CMB + 2dFGRS. Fits to CMB data alone reveal two well-known primary degeneracies. For models including a possible tensor component, there is tensor degeneracy (Efstathiou 2002) between increasing tensors, blue tilt, increased baryon density and lower CDM density. For both scalar-only and with-tensor models, there is a degeneracy related to the geometrical degeneracy present when non-flat models are considered, arising from models with similar observed CMB peak locations (cf. Efstathiou & Bond 1999). In Section 4 we discuss this degeneracy further and explain how it may be easily understood via the horizon angle, and described by the simple relation $\Omega_m h^{3.4} = $ constant.

Section 5 considers a possible extension of our standard cosmological model, allowing the equation of state parameter w of the vacuum energy component to vary. By combining the CMB data, the 2dFGRS data and an external constraint on the Hubble constant h, we are able to constrain w. Finally, in Section 6, we discuss the range of CMB angular power spectral values allowed by the present CMB and 2dFGRS data within the standard class of flat models.

2 THE CMB DATA

Recent key additions to the field of CMB observations come from the VSA (Scott et al. 2002), which boasts a smaller calibration error than previous experiments, and the CBI (Pearson et al. 2002; Mason et al. 2002), which has extended observations to smaller angles (larger ℓ). These data sets add to results from BOOMERaNG (Netterfield et al. 2002), Maxima (Lee et al. 2001) and DASI (Halverson et al. 2002), amongst others. Rather than compare models with each of these data sets individually, it is expedient to combine the data prior to analysis. This combination often has the advantage of allowing a consistency check between the individual data sets (e.g. Wang, Tegmark & Zaldarriaga 2002). However, care must be taken to ensure that additional biases are not introduced into the compressed data set, and that no important information is lost.

In the following we consider *COBE*, BOOMERaNG, Maxima, DASI, VSA and CBI data sets. The BOOMERaNG data of Netterfield et al. (2002) and the Maxima data of Lee et al. (2001) were used assuming the data points to be independent, and have window functions well described by top-hats. The $\ell < 2000$ CBI mosaic field data were used assuming that the only significant correlations arise between neighbouring points that are anticorrelated at the 16 per cent level as discussed in Pearson et al. (2002). Window functions for these data were assumed to be Gaussian with small negative side lobes extending into neighbouring bins approximately matched to fig. 11 of Pearson et al. (2002). We also consider the VSA data of Scott et al. (2002), the DASI data of Halverson et al. (2002), and the *COBE* data compilation of Tegmark (1996), for which the window functions and covariance matrices are known, where appropriate. The calibration uncertainties used are presented in Table 1, and the data sets are shown in Fig. 1. In total, there are six data sets, containing 68 power measurements.

In order to combine these data sets, we have fitted a model for the true underlying CMB power spectrum, consisting of power values at a number of ℓ values (or nodes). Between these nodes we interpolate the model power spectrum using a smooth Spline3 algorithm (Press et al. 1992). The assumption of smoothness is justified because we aim to compare CMB data with CDM models calculated using CMBFAST (Seljak & Zaldarriaga 1996). Internally, this

Table 1. Best-fitting relative power calibration corrections for the experiments considered are compared with expected rms errors. In addition, we recover a best-fitting beam error for BOOMERaNG of $+0.4$ per cent, measured relative to the first data point in the set, and $+0.07$ per cent for Maxima.

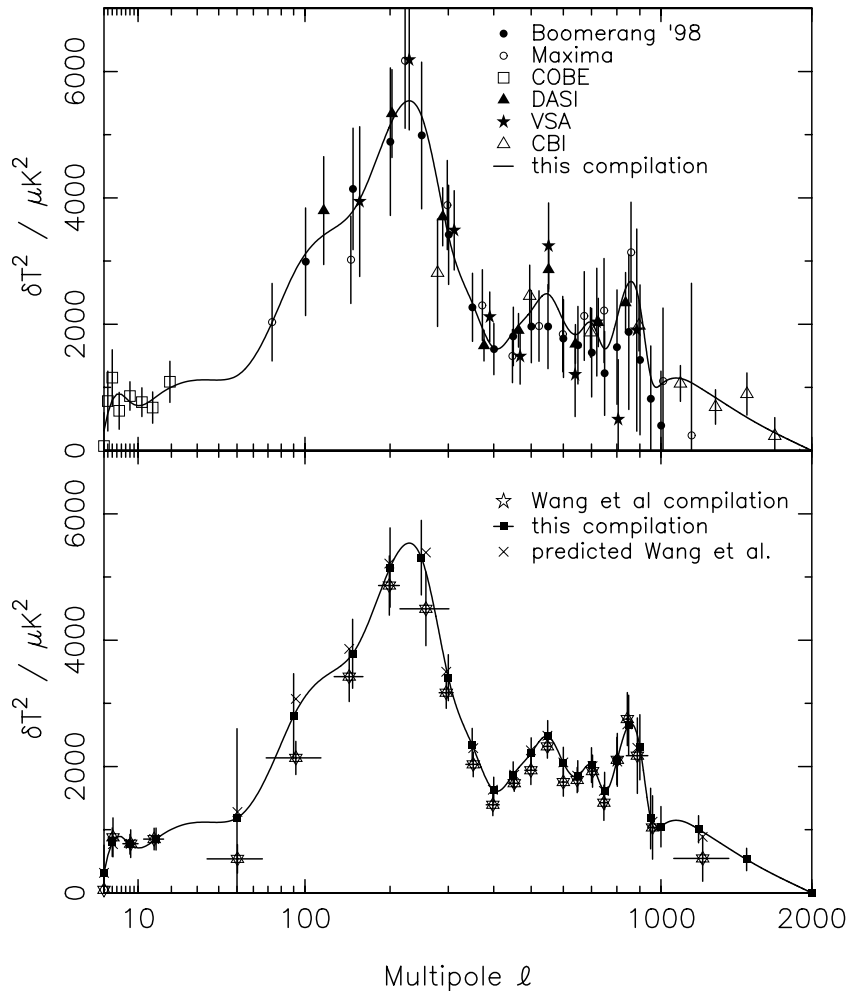| Experiment	Power calibration error	
	Best fit (per cent)	rms (per cent)
BOOMERaNG	-13.5	20
Maxima	$+1.6$	8
DASI	$+0.9$	8
VSA	-0.3	7
CBI	$+0.7$	10

Figure 1. Top panel: the compilation of recent CMB data used in our analysis (see the text for details). The solid line shows the result of a maximum-likelihood fit to these data, allowing for calibration and beam uncertainty errors in addition to intrinsic errors. Each observed data set has been shifted by the appropriate best-fitting calibration and beam correction. Bottom panel: the solid line again shows our maximum-likelihood fit to the CMB power spectrum now showing the nodes (the points at which the amplitude of the power spectrum was estimated) with approximate errors calculated from the diagonal elements of the covariance matrix (solid squares). These data are compared with the compilation of Wang et al. (2002) (stars) and the result of convolving our best-fitting power with the window function of Wang et al. (crosses). In order to show the important features in the CMB angular power spectrum plots we present in this paper we have chosen to scale the x-axis by $(\log \ell)^{5/2}$.

code evaluates the CMB power spectrum only at a particular set of ℓ values, which are subsequently Spline3 interpolated to cover all multipoles. It is therefore convenient to use as our parameters the CMB power values at the same nodes used by CMBFAST in the key regime $150 \leqslant \ell \leqslant 1000$. Using the same smoothing algorithm and nodes for our estimate of the true power spectrum, we ensure that no additional assumptions are made in the data compilation compared with the models to be tested. For $\ell < 150$ and $\ell > 1000$ the data points are rather sparsely distributed, and we only selected a few ℓ values at which to estimate the power. The best-fitting amplitude of the power spectrum at an extra node at $\ell = 2000$ was determined in our fit to the observed CMB data, in order for the shape of the interpolated curve around $\ell = 1500$ to have the correct form. This was subsequently removed from the analysis, and models and data were only compared for $\ell \leqslant 1500$. In addition to requiring no interpolation in CMBFAST, this method of compression has a key advantage for our analysis. Normally, CMB data are expressed as bandpowers, in which one specifies the result of convolving the CMB power spectrum with some kernel. This remains true of some previous CMB

data compilations (e.g. Wang et al. 2002). In contrast, we estimate the true power spectrum at a given ℓ directly, so that no convolution step is required. This means that parameter space can be explored more quickly and efficiently.

Given a set of nodal values, we form an interpolated model power spectrum, convolve with the window function of each observed data point and maximized the likelihood with respect to the nodal values (assuming Gaussianity – see Bond, Jaffe & Knox 2000 for a discussion of the possible effect of this approximation). Calibration errors and beam uncertainties were treated as additional independent Gaussian parameters, and were combined into the final likelihood, as well as being used to correct the data. The resulting best-fitting calibration and beam errors are compared with the expected rms values in Table 1.

In agreement with Wang et al. (2002), we find a negative best-fitting BOOMERaNG calibration correction (13 per cent in power), caused by matching data sets in the regime $300 < \ell < 500$. Applying this correction (included in the data points in Fig. 1) slightly decreases the amplitude of the first peak. Nevertheless, our combined

Table 2. Recovered best-fitting power spectrum values with rms values given the six data sets analysed.

ℓ	δT^2 (μK^2)	rms error (μK^2)
2	314	443
4	803	226
8	770	156
15	852	174
50	1186	1414
90	2796	673
150	3784	546
200	5150	627
250	5306	590
300	3407	364
350	2339	265
400	1627	205
450	1873	202
500	2214	240
550	2479	249
600	2061	245
650	1849	244
700	2023	274
750	1614	295
800	2089	373
850	2654	475
900	2305	515
950	1178	480
1000	1048	320
1200	1008	214
1500	530	178

power values are systematically higher than in the compilation of Wang et al. (see the lower panel of Fig. 1). This derives partly from the inclusion of extra data, but also results from a bias in the analysis method of Wang et al. They use the observed power values to estimate the error in the data, rather than the true power at that multipole (which we estimate from our model). A low observational point is thus given a spuriously low error, and this is capable of biasing the averaged data to low values.

The final best-fitting power spectrum amplitudes given the six data sets analysed are presented in Table 2, with the corresponding ℓ-values of the nodes and rms errors. Formally, this fit gave $\chi^2_{\min} = 31.9$, given 34 degrees of freedom (there are 68 data points, and we estimate 27 power spectrum values, five calibration and two beam corrections). This result demonstrates that the different data sets are broadly consistent after allowing for calibration and beam uncertainty. The Hessian matrix of the likelihood provides an estimate of the inverse covariance matrix for the power spectrum estimates. This was calculated numerically and is available, together with the averaged data, from http://www.roe.ac.uk/~wjp/. As emphasized previously, these are estimates of the true power at the ℓ values given and therefore do not require window functions. In the following section we use these CMB results to constrain flat cosmological models.

3 COSMOLOGICAL MODELS

3.1 Parameter space

In the following we parametrize flat cosmological models with seven parameters (plus two amplitudes): these are the physical baryon den-

Table 3. The distribution of parameters (defined in the text) in the $\sim 2 \times 10^8$ flat cosmological models considered in this paper. The grid used was linear in each parameter between the limits given in order to simplify the marginalization assuming a uniform prior on each.

Parameter	Min	Max	Grid size
$\Omega_b h^2$	0.01	0.04	25
$\Omega_c h^2$	0.05	0.22	25
h	0.40	1.00	25
τ	0.00	0.10	2
n_s	0.80	1.30	25
n_t	-0.20	0.30	10
r	0.00	1.00	25

sity[1] $\Omega_b h^2$, the physical CDM density $\Omega_c h^2$, the Hubble constant h, the optical depth to the last scattering surface τ, the scalar spectral index n_s, the tensor spectral index n_t and the tensor-to-scalar ratio r. The tensor-to-scalar ratio r is defined as in Efstathiou et al. (2002): the scalar and tensor C_ℓ are normalized so that

$$\frac{1}{4\pi} \sum_{\ell=2}^{1000} (2\ell + 1)\hat{C}_\ell^S = (4 \times 10^{-5})^2, \tag{1}$$

$$\frac{1}{4\pi} \sum_{\ell=2}^{50} (2\ell + 1)\hat{C}_\ell^T = (2 \times 10^{-5})^2. \tag{2}$$

C_ℓ is then given by $C_\ell = Q^2(\hat{C}_\ell^S + r\hat{C}_\ell^T)$, where Q^2 is the normalization constant. We marginalize over both this and the amplitude of the 2dFGRS power spectra in order to avoid complications caused by galaxy biasing and redshift space distortions (Lahav et al. 2002).

CMB angular power spectra have been calculated using CMBFAST (Seljak & Zaldarriaga 1996) for a grid of $\sim 2 \times 10^8$ models. For ease of use, a uniform grid was adopted with a varying resolution in each of the parameters (details of this grid are presented in Table 3). Likelihoods were calculated by fitting these models to the reduced CMB data set presented in Section 2. Similarly, large-scale structure (LSS) power spectra were calculated for the relevant models using the fitting formula of Eisenstein & Hu (1998), and were convolved with the window function of the 2dFGRS sample, before being compared with the 2dFGRS data as in Percival et al. (2001).

In order to constrain parameters, we wish to determine the probability of each model in our grid given the available CMB and 2dF-GRS data. However, we can only easily calculate the probability of the data given each model. In order to convert between these probabilities using Bayes' theorem, we need to adopt a prior probability for each model or parameter. In this work, we adopt a uniform prior for the parameters discussed above between the limits in Table 3. i.e. we assume that the prior probability of each model in the grid is the same. Assuming a uniform prior for physically motivated parameters is common in the field, although not often explicitly mentioned. Note that the constraints placed by the current data are tight compared with the prior, and that the biases induced by this choice are therefore relatively small.

The likelihood distribution for a single parameter, or for two parameters can be calculated by marginalizing the estimated

---

[1] As usual, Ω_b and Ω_c are the densities of baryons and CDM in units of the critical density, and h is the Hubble constant in units of $100 \text{ km s}^{-1} \text{ Mpc}^{-1}$. 'Derived' parameters include the matter density $\Omega_m = \Omega_c + \Omega_b$ and $\Omega_\Lambda = 1 - \Omega_m$.
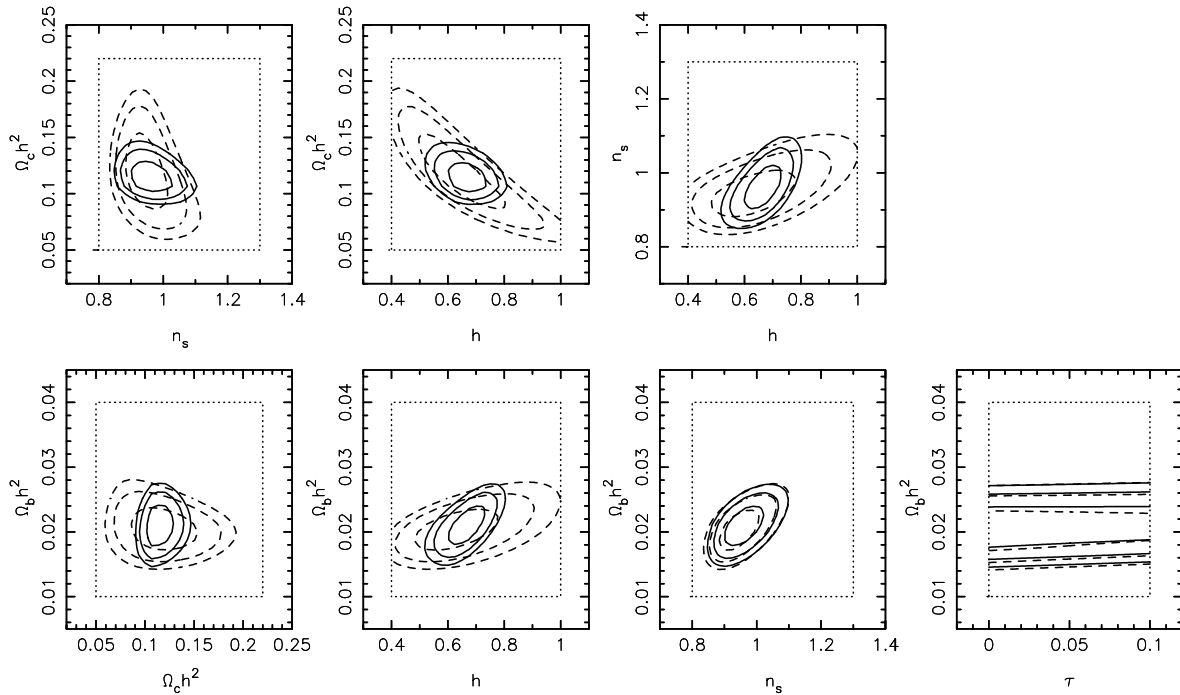
Figure 2. Two parameter likelihood surfaces for scalar-only models. Contours correspond to changes in the likelihood from the maximum of $2\Delta \ln \mathcal{L} = 2.3, 6.0, 9.2$. Dashed contours are calculated by only fitting to the CMB data, solid contours by jointly fitting the CMB and 2dFGRS data. Dotted lines show the extent of the grid used to calculate the likelihoods.

probability of the model given the data over all other parameters. Because of the grid adopted in this work, we can perform this marginalization by simply averaging the $\mathcal{L}$ values calculated at each point in the grid.

In Fig. 2 we present two-parameter likelihood contour plots (marginalized over the remaining parameters) for the subset of scalar-only models, i.e. r fixed at 0. For these scalar-only models, we choose to plot τ only against $\Omega_b h^2$ as τ is poorly constrained by the CMB data, and has no degeneracies with the other parameters. In Fig. 3 we present two-parameter likelihood contour plots (marginalized over the remaining parameters) for models allowing a tensor component. The spectral index of the tensor contribution is poorly constrained by the CMB data so, as for τ, we only show one plot with this parameter.

Figs 2 and 3 reveal two key directions in parameter space that the CMB data have difficulty constraining. When a tensor component is included, we have the tensor degeneracy – a trade-off between increasing tensors, increasing n_s, increasing $\Omega_b h^2$ and decreasing $\Omega_c h^2$ (for more detail see Efstathiou 2002). In addition, in both the scalar-only and with-tensor cases, there is a degeneracy between $\Omega_c h^2$ and h, which results in the Hubble parameter h being poorly constrained by the CMB data alone. This degeneracy is discussed in detail in the next section.

We note that nearly all of the likelihood is contained well within our prior regions, except for the case of tensor models with CMB-only data in Fig. 3: here there is a region allowed by CMB outside our priors with high tensor fraction, $h > 1$, $n_s \simeq 1.3$, $\Omega_c h^2 \simeq 0.06$. These parameters are ruled out by many observations apart from 2dFGRS, so the truncation is not a concern.

3.2 Results

The recovered mean and standard rms error calculated for each parameter (except τ which is effectively unconstrained) are given in

Table 4. What is striking is how well specified many of the parameters are.

The general features are as follows: changing from the compilation of Wang et al. to our compilation shrinks the error bars slightly (owing to VSA and CBI), but the central values are similar except for a slight shift in n_s. Allowing tensors widens the error bars and causes modest shifts in central values (the best fit has a zero tensor fraction, but the fact that r must be non-negative explains the shifts). The CMB data alone constrains $\Omega_b h^2$ and n_s well and $\Omega_c h^2$ quite well, but Ω_m and h less well. Adding the 2dFGRS data shrinks the errors on $\Omega_c h^2$, h and thus Ω_m and Ω_b/Ω_m by more than a factor of 2.

The most restrictive case is the set of scalar-only models. These yield $h = 0.665$ with only a 7 per cent error, which is substantially better than any other method. The matter density parameter comes out at $\Omega_m = 0.313$, with a rather larger error of 18 per cent; errors on h and Ω_m are anticorrelated so the physical matter density is well determined, $\Omega_m h^2 = 0.136 \pm 7$ per cent. In Section 4 below we show that this is because the CMB data measure the combination $\Omega_m h^3$ very accurately, so that an accurate measurement of Ω_m requires h to be known almost exactly.

Moving from matter content to the fluctuation spectrum, the scalar-only results give a tantalizing hint of red tilt, with $n_s = 0.963 \pm 0.042$. Current data are thus within a factor of 2 of the precision necessary to detect plausible degrees of tilt (e.g. $n_s = 0.95$ for $\lambda\phi^4$ inflation; see Section 8.3 of Liddle & Lyth 2000). Inflation of course cautions against ignoring tensors, but it would be a great step forward to rule out an $n_s = 1$ scalar-only model.

Including the possibility of tensors changes these conclusions only moderately. The errors on h and Ω_m hardly alter, whereas the error on n_s rises to 0.066. The preferred model has $r = 0$, although this is rather poorly constrained. Marginalizing over the other parameters, we obtain a 95 per cent confidence upper limit of $r < 0.7$. One way of ruling out the upper end of this range may be to note that
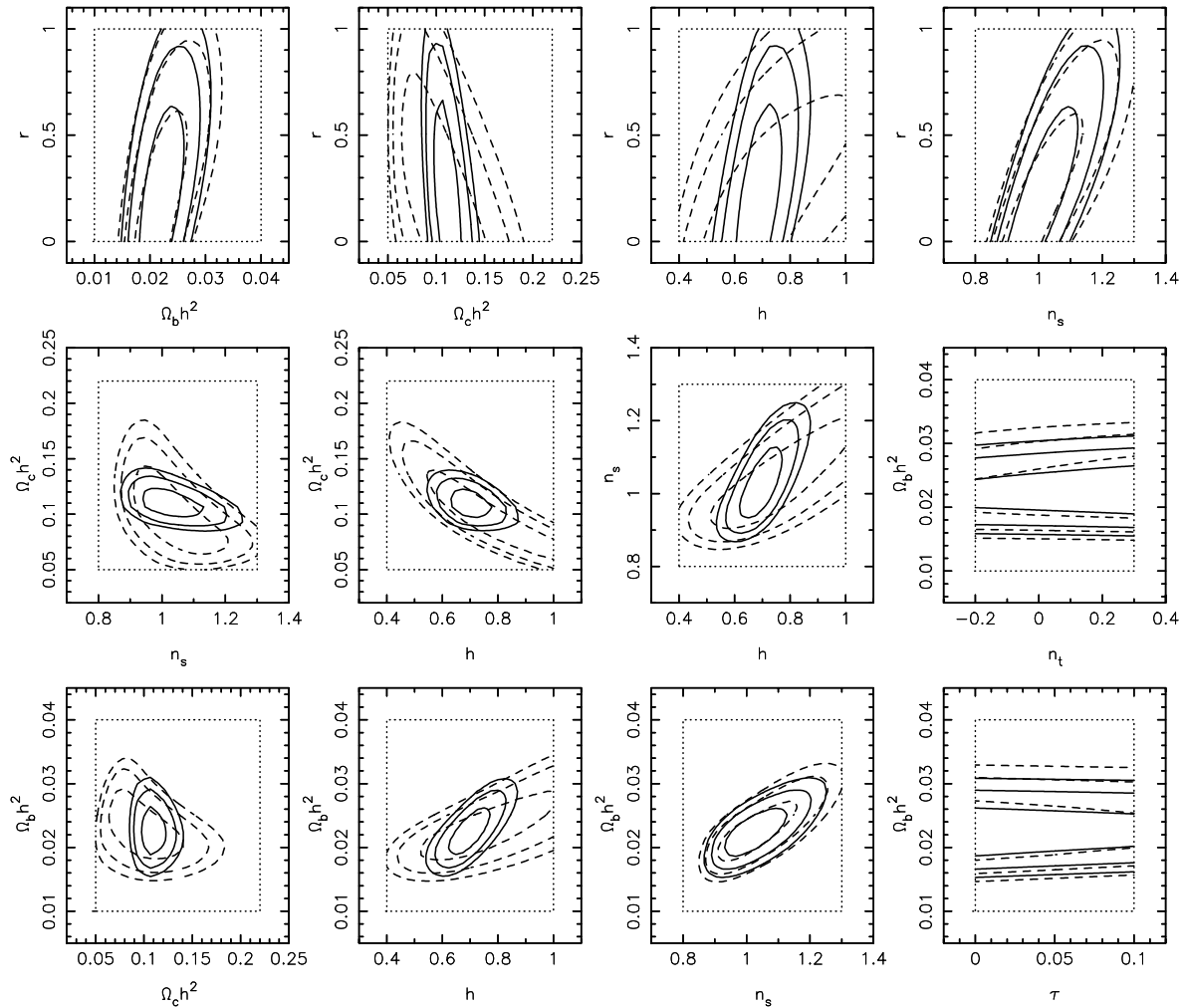
Figure 3. As in Fig. 2, but now considering a wider class of models that possibly include a tensor component.

such tensor-dominated models predict a rather low normalization for the present-day mass fluctuations, as we now discuss.

3.3 Normalization

An advantage of the new CMB data included here is that the most recent experiments have a rather small calibration uncertainty. It is therefore possible to obtain precise values for the overall normalization of the power spectrum. As usual, we take this to be specified by σ_8, the rms density contrast averaged over spheres of $8\,h^{-1}$ Mpc radius. For the scalar-only grid of models shown in Fig. 2, this yields

$$\sigma_8 = (0.72 \pm 0.03 \pm 0.02)\exp(\tau). \tag{3}$$

The first error figure is the 'theory error': the uncertainty in σ_8 that arises because the conversion between the observed C_ℓ and the present $P(k)$ depends on the uncertain values of Ω_m, etc. The second error figure represents the uncertainty in the normalization of the C_ℓ data (see Fig. 7 in Section 6). The total error in σ_8 is the sum in quadrature of these two figures.

This result confirms with greater precision our previous conclusions that the allowed scalar-only models prefer a relatively low normalization (Efstathiou et al. 2002; Lahav et al. 2002). As dis-

cussed by Lahav et al. (2002), a figure of $\sigma_8 = 0.72$ is consistent with the relatively wide range of estimates from the abundance of rich clusters, but is lower than the $\sigma_8 \simeq 0.9$ for $\Omega_m \simeq 0.3$ preferred by weak lensing studies. The obvious way to reconcile these figures is via the degenerate dependence of σ_8 on τ. The lowest plausible value for this is $\tau = 0.05$, corresponding to reionization at $z_r = 8$ for the parameters given here. To achieve $\sigma_8 = 0.9$ requires $\tau = 0.22$, or reionization at $z_r = 22$, which is somewhat higher than conventional estimates ($z_r < 15$; see, e.g., Loeb & Barkana 2001). Additional evidence in this direction comes from the possible first detection of Sunyaev–Zeldovich anisotropies at $\ell > 200$ by the CBI (Mason et al. 2002). This signal is claimed to require $\sigma_8 \simeq 1$ (Bond et al. 2002), which would raise z_r to almost 30. Further scrutiny of these independent estimates for σ_8 will be required before one can claim evidence for first object formation at extreme redshifts, but this is an exciting possibility.

Finally, we note that these problems are sharpened if the CMB power spectrum has a substantial tensor component. As shown by Efstathiou et al. (2002), the model with the maximal allowed tensor fraction ($r = 0.6$) has a normalization lower by a factor 1.18 than the best scalar-only model. This pushes z_r to almost 40 for $\sigma_8 = 1$, which starts to become implausibly high, even given the large uncertainties associated with the modelling of reionization.

Table 4. The recovered mean and root mean square (rms) error for each parameter, calculated by marginalizing over the remaining parameters. Results are presented for scalar-only and scalar + tensor models, and for CMB data only or CMB and 2dFGRS power spectrum data. To reduce round-off error, means and rms errors are quoted to an accuracy such that the rms error has two significant figures. We also present constraints on some of the possible derived parameter combinations. (Note that because of the marginalization, the maximum-likelihood values of 'derived' parameters, e.g. Ω_m are not simply ratios of the ML values for each 'independent' parameter.)

	Parameter	Results: scalar only		Results: with tensor component	
		CMB	CMB + 2dFGRS	CMB	CMB + 2dFGRS
	$\Omega_b h^2$	0.0205 ± 0.0022	0.0210 ± 0.0021	0.0229 ± 0.0031	0.0226 ± 0.0025
	$\Omega_c h^2$	0.118 ± 0.022	0.1151 ± 0.0091	0.100 ± 0.023	0.1096 ± 0.0092
	h	0.64 ± 0.10	0.665 ± 0.047	0.75 ± 0.13	0.700 ± 0.053
Using the	n_s	0.950 ± 0.044	0.963 ± 0.042	1.040 ± 0.084	1.033 ± 0.066
CMB data	n_t	−	−	0.09 ± 0.16	0.09 ± 0.16
compilation	r	−	−	0.32 ± 0.23	0.32 ± 0.22
of Section 2	Ω_m	0.38 ± 0.18	0.313 ± 0.055	0.25 ± 0.15	0.275 ± 0.050
	$\Omega_m h$	0.226 ± 0.069	0.206 ± 0.023	0.174 ± 0.063	0.190 ± 0.022
	$\Omega_m h^2$	0.139 ± 0.022	0.1361 ± 0.0096	0.123 ± 0.022	0.1322 ± 0.0093
	Ω_b / Ω_m	0.152 ± 0.031	0.155 ± 0.016	0.193 ± 0.048	0.172 ± 0.021
	$\Omega_b h^2$	0.0209 ± 0.0022	0.0216 ± 0.0021	0.0233 ± 0.0032	0.0233 ± 0.0025
	$\Omega_c h^2$	0.124 ± 0.024	0.1140 ± 0.0088	0.107 ± 0.025	0.1091 ± 0.0089
	h	0.64 ± 0.11	0.682 ± 0.046	0.74 ± 0.14	0.719 ± 0.054
Using the	n_s	0.987 ± 0.047	1.004 ± 0.047	1.073 ± 0.087	1.079 ± 0.073
Wang et al. (2002)	n_t	−	−	0.03 ± 0.15	0.03 ± 0.15
compilation	r	−	−	0.25 ± 0.21	0.27 ± 0.20
	Ω_m	0.41 ± 0.20	0.296 ± 0.051	0.28 ± 0.17	0.261 ± 0.048
	$\Omega_m h$	0.240 ± 0.076	0.200 ± 0.021	0.189 ± 0.071	0.185 ± 0.021
	$\Omega_m h^2$	0.145 ± 0.024	0.1356 ± 0.0092	0.131 ± 0.024	0.1324 ± 0.0088
	Ω_b / Ω_m	0.149 ± 0.033	0.160 ± 0.016	0.186 ± 0.049	0.177 ± 0.021

4 THE HORIZON ANGLE DEGENERACY

In this section we explore the degeneracy observed in Figs 2 and 3 between $\Omega_c h^2$ and h. This is related (but not identical) to the geometrical degeneracy that exists when non-flat models are considered, and we now show that it is very closely related to the location of the acoustic peaks. Below, we first review the basics of the geometrical degeneracy; secondly, note why this is only weakly broken by the flatness assumption, and thirdly give a simple heuristic argument why this degeneracy approximately follows a contour of nearly constant $\Omega_m h^3$.

4.1 The geometrical degeneracy

The 'geometrical degeneracy' in the CMB is well known (Bond, Efstathiou & Tegmark 1997; Zaldarriaga, Spergel & Seljak 1997; Efstathiou & Bond 1999). If we take a family of models with fixed initial perturbation spectra, fixed physical densities $\omega_m \equiv \Omega_m h^2$, $\omega_b \equiv \Omega_b h^2$, and vary both Ω_Λ and the curvature Ω_k to keep a fixed value of the angular size distance to last scattering, then the resulting CMB power spectra are identical (except for the integrated Sachs–Wolfe effect at low multipoles, which is hidden in cosmic variance, and second-order effects at high ℓ). This degeneracy occurs because the physical densities ω_m, ω_b control the structure of the perturbations in physical Mpc at last scattering, while curvature and Λ (plus ω_m) govern the proportionality between the length at last scattering and the observed angle. Note that h is a 'derived' parameter in the above set, via $h = [\omega_m/(1 - \Omega_k - \Omega_\Lambda)]^{1/2}$, so the geometrical degeneracy is broken by an external measurement of h.

4.2 The flat-universe case

Assuming a flat universe, $\Omega_k = 0$, thus also breaks the geometrical degeneracy. However, as noted by, for example, Efstathiou & Bond

(1999), and investigated below, there is a closely related degeneracy based on varying two free parameters (chosen from Ω_m, ω_m, h, Ω_Λ) so as to almost preserve the locations of the first few CMB acoustic peaks. This is illustrated in Fig. 4, where the likelihood contours in the (Ω_m, h) plane for CMB-only data form a long and narrow 'banana' with its long axis at approximately constant $\Omega_m h^3$. The banana is surprisingly narrow in the other direction; this means that $\Omega_m h^3$ is determined to approximately 12 per cent (1σ) by the CMB data.

This 'banana' is similar in form to the line in fig. 4 of Efstathiou & Bond (1999), though it is different in detail because they used simulations with $\omega_m = 0.25$. It is also similar to that in fig. 1 of Knox, Christensen & Skordis (2001) as expected. However, both of those previous papers presented the degeneracy in the (Ω_Λ, h) plane; although this is just a mirror-image of the (Ω_m, h) plane, it is less intuitive (e.g. changing Ω_Λ alters observables that have no explicit Λ dependence, via the constraint $\Omega_m = 1 - \Omega_\Lambda$), so the simple $\Omega_m h^3$ dependence has not been widely recognized.

4.3 Peak locations and the sound horizon

The locations ℓ_m of the first few CMB acoustic peaks may be conveniently expressed (e.g. Hu et al. 2001; Knox et al. 2001) as

$$\ell_m = \ell_A(m - \phi_m), \qquad m = 1, 2, 3 \tag{4}$$

$$\ell_A \equiv \pi/\theta_S \tag{5}$$

$$\theta_S \equiv \frac{r_S(z_*)}{D_A(z_*)}, \tag{6}$$

where r_S is the sound horizon size at last scattering (redshift z_*), D_A is the angular diameter distance to last scattering, therefore θ_S is the 'sound horizon angle' and ℓ_A is the 'acoustic scale'. For any
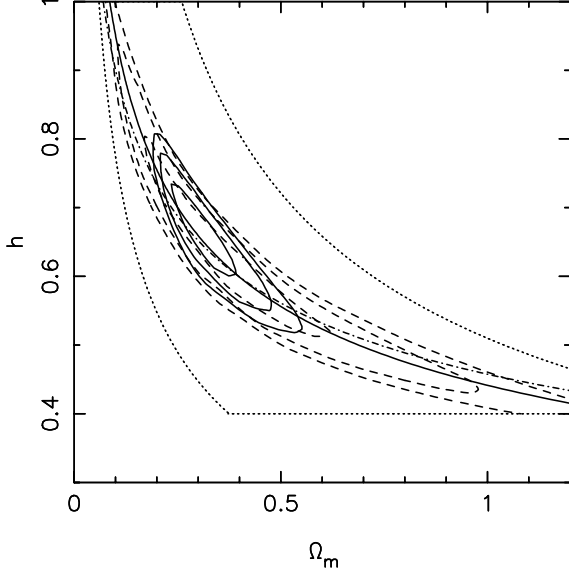
Figure 4. Likelihood contours for Ω_m against h for scalar-only models, plotted as in Fig. 2. Variables were changed from $\Omega_b h^2$ and $\Omega_c h^2$ to Ω_m and Ω_b/Ω_m, and a uniform prior was assumed for Ω_b/Ω_m covering the same region as the original grid. The extent of the grid is shown by the dotted lines. The dot-dashed line follows the locus of models through the likelihood maximum with constant $\Omega_m h^{3.4}$. The solid line is a fit to the likelihood valley and shows the locus of models with constant $\Omega_m h^{3.0}$ (see the text for details).

given model, the CMB peak locations $\ell_m (m = 1, 2, 3)$ are given by numerical computation, and then equation (4) defines the empirical 'phase shift' parameters ϕ_m. Hu et al. (2001) show that the ϕ_m are weakly dependent on cosmological parameters and $\phi_1 \sim 0.27$, $\phi_2 \sim 0.24$, $\phi_3 \sim 0.35$. Extensive calculations of the ϕ_m are given by Doran & Lilley (2002).

Therefore, although θ_S is not directly observable, it is very simple to compute and very tightly related to the peak locations, hence its use below. Knox et al. (2001) note a 'coincidence' that θ_S is tightly correlated with the age of the universe for flat models with parameters near the 'concordance' values, and use this to obtain an accurate age estimate assuming flatness.

4.4 A heuristic explanation

Here we provide a simple heuristic explanation for why θ_S and hence the ℓ_ms are primarily dependent on the parameter combination $\Omega_m h^{3.4}$.

Of the four 'FRW' parameters Ω_m, ω_m, h, Ω_Λ, only two are independent for flat models, and we can clearly choose any pair except for $(\Omega_m, \Omega_\Lambda)$. The standard choice in CMB analyses is $(\omega_m, \Omega_\Lambda)$, while for non-CMB work the usual choice is (Ω_m, h). However, in the following we take ω_m and Ω_m to be the independent parameters (thus h, Ω_Λ are derived); this looks unnatural but separates more clearly the low-redshift effect of Ω_m from the pre-recombination effect of ω_m. We take ω_b as fixed unless otherwise specified (its effect here is small).

We first note that the present-day horizon size for flat models is well approximated by (Vittorio & Silk 1985)

$$r_H(z = 0) = \frac{2c}{H_0} \Omega_m^{-0.4} = 6000 \, \text{Mpc} \, \frac{\Omega_m^{0.1}}{\sqrt{\omega_m}}. \tag{7}$$

(The distance to last scattering is ~ 2 per cent smaller than the above because of the finite redshift of last scattering.) Therefore, if we increase Ω_m while keeping ω_m fixed, the shape and relative heights of the CMB peaks are preserved but the peaks move slowly rightwards (increasing ℓ) proportional to $\Omega_m^{0.1}$. (Equivalently, the Efstathiou–Bond $\mathcal{R}$ parameter for flat models is well approximated by $1.94 \, \Omega_m^{0.1}$.)

This slow variation of $\ell_A \propto \Omega_m^{0.1}$ at fixed ω_m explains why the geometrical degeneracy is only weakly broken by the restriction to flat models: a substantial change in Ω_m at fixed ω_m moves the peaks only slightly, so a small change in ω_m can alter the sound horizon length $r_S(z_*)$ and bring the peaks back to their previous angular locations with only a small change in relative heights. We now give a simplified argument for the dependence of r_S on ω_m.

The comoving sound horizon size at last scattering is defined by (e.g. Hu & Sugiyama 1995)

$$r_S(z_*) \equiv \frac{1}{H_0 \Omega_m^{1/2}} \int_0^{a_*} \frac{c_S}{(a + a_{eq})^{1/2}} \, da, \tag{8}$$

where the vacuum energy is neglected at these high redshifts; the expansion factor $a \equiv (1 + z)^{-1}$ and a_*, a_{eq} are the values at recombination and matter–radiation equality, respectively. Thus r_S depends on ω_m and ω_b in several ways:

(i) the expansion rate in the denominator depends on ω_m via a_{eq};

(ii) the speed of sound c_S depends on the baryon/photon ratio via $c_S = c/\sqrt{3(1 + R)}$, $R = 30\,496 \, \omega_b \, a$;

(iii) the recombination redshift z_* depends on both the baryon and matter densities ω_b, ω_m in a fairly complex way.

Since we are interested mainly in the derivatives of r_S with ω_m, ω_b, it turns out that (i) above is the dominant effect. The dependence (iii) of z_* on ω_m, ω_b is slow. Concerning (ii), for baryon densities $\omega_b \simeq 0.02$, c_S declines smoothly from $c/\sqrt{3}$ at high redshift to $0.80 \, c/\sqrt{3}$ at recombination. Therefore, to a reasonable approximation we may take a fixed 'average' $c_S \simeq 0.90 \, c/\sqrt{3}$ outside the integral in equation (8), and take a fixed z_*, giving the approximation

$$r_S(z_*) \simeq \frac{0.90}{\sqrt{3}} \, r_H \, (z = 1100), \tag{9}$$

where r_H is the light horizon size; this approximation is very accurate for all ω_m considered here and $\omega_b \simeq 0.02$. For other baryon densities, multiplying the right-hand side of equation (9) by $(\omega_b/0.02)^{-0.07}$ is a refinement. [Around the concordance value $\omega_b = 0.02$, effects (ii) and (iii) partly cancel, because increasing ω_b lowers the speed of sound but also delays recombination i.e. increases a_*.]

From above, the (light) horizon size at recombination is

$$r_H(z_*) = \frac{c}{H_0 \Omega_m^{1/2}} \int_0^{a_*} \frac{1}{(a + a_{eq})^{1/2}} \, da$$
$$= \frac{6000 \, \text{Mpc}}{\sqrt{\omega_m}} \sqrt{a_*} \left[\sqrt{1 + (a_{eq}/a_*)} - \sqrt{a_{eq}/a_*} \right]. \tag{10}$$

Dividing by $D_A \simeq 0.98 \, r_H \, (z = 0)$ from equation (7) gives the angle subtended today by the light horizon,

$$\theta_H \simeq 1.02 \, \frac{\Omega_m^{-0.1}}{\sqrt{1 + z_*}} \left(\sqrt{1 + \frac{a_{eq}}{a_*}} - \sqrt{\frac{a_{eq}}{a_*}} \right). \tag{11}$$

Inserting $z_* = 1100$ and $a_{eq} = (23\,900 \, \omega_m)^{-1}$, we have

$$\theta_H = \frac{1.02 \, \Omega_m^{-0.1}}{\sqrt{1101}}$$
$$\times \left[\sqrt{1 + 0.313 \left(\frac{0.147}{\omega_m} \right)} - \sqrt{0.313 \left(\frac{0.147}{\omega_m} \right)} \right], \tag{12}$$

and $\theta_S \simeq \theta_H \times 0.9/\sqrt{3}$ from equation (9). This remarkably simple result captures most of the parameter dependence of CMB peak locations within flat ΛCDM models. Note that the square brackets in equation (12) tends (slowly) to 1 for $a_{eq} \ll a_*$ i.e. $\omega_m \gg 0.046$; thus it is the fact that matter domination occurred not much earlier than recombination that leads to the significant dependence of θ_H on ω_m and hence h.

Differentiating equation (12) near a fiducial $\omega_m = 0.147$ gives

$$\left. \frac{\partial \ln \theta_H}{\partial \ln \Omega_m} \right|_{\omega_m} = -0.1,$$

$$\left. \frac{\partial \ln \theta_H}{\partial \ln \omega_m} \right|_{\Omega_m} = \frac{1}{2}\left(1 + \frac{a_*}{a_{eq}}\right)^{-1/2} = +0.24, \qquad (13)$$

and the same for derivatives of $\ln \theta_S$ from the approximation above. In terms of (Ω_m, h) this gives

$$\left. \frac{\partial \ln \theta_H}{\partial \ln \Omega_m} \right|_{h} = +0.14, \quad \left. \frac{\partial \ln \theta_H}{\partial \ln h} \right|_{\Omega_m} = +0.48, \qquad (14)$$

in good agreement with the numerical derivatives of ℓ_A in equation (A15) of Hu et al. (2001). Also note the sign difference between the two $\partial/\partial \ln \Omega_m$ values above.

Thus for moderate variations from a 'fiducial' model, the CMB peak locations scale approximately as $\ell_m \propto \Omega_m^{-0.14} h^{-0.48}$, i.e. the condition for constant CMB peak location is well approximated as $\Omega_m h^{3.4} = $ constant. This condition can also be written as $\omega_m \Omega_m^{-0.41} = $ constant, and we see that, along such a contour, ω_m varies as $\Omega_m^{0.41}$, and hence the peak heights are slowly varying and the overall CMB power spectrum is also slowly varying.

There are four approximations used for θ_S above: one in equation (7), two (constant c_s and z_*) in equation (9), and finally the $\Omega_m h^{3.4}$ line is a first-order (in log) approximation to a contour of constant equation (12). Checking against numerical results, we find that each of these causes up to 1 per cent error in θ_S, but they partly cancel: the exact value of θ_S varies by < 0.5 per cent along the contour $h = 0.7(\Omega_m/0.3)^{-1/3.4}$ between $0.1 \leqslant \Omega_m \leqslant 1$. The peak heights shift the numerical degeneracy by more than this (see below), so the error is unimportant.

A line of constant $\Omega_m h^{3.4}$ is compared with the likelihood surface recovered from the CMB data in Fig. 4. In order to calculate the required likelihoods, we have made a change of variables from ω_b and $\Omega_c h^2$ to Ω_m and Ω_b/Ω_m, and have marginalized over the baryon fraction assuming a uniform prior in Ω_b/Ω_m covering the limits of the grid used. As expected, the degeneracy observed when fitting the CMB data alone is close to a contour of constant ℓ_A and hence constant θ_H. However, information concerning the peak heights does alter this degeneracy slightly; the relative peak heights are preserved at constant ω_m, hence the actual likelihood ridge is a 'compromise' between constant peak location (constant $\Omega_m h^{3.4}$) and constant relative heights (constant $\Omega_m h^2$); the peak locations have more weight in this compromise, leading to a likelihood ridge along $\Omega_m h^{3.0} \simeq $ constant. This is shown by the solid line in Fig. 4. To demonstrate where this alteration is coming from, we have plotted three scalar-only models in the top panel of Fig. 5. These models lie approximately along the line of constant $\Omega_m h^{3.4}$, with $\Omega_m = 0.93, 0.36, 0.10$. Parameters other than Ω_m and h have been adjusted to fit the CMB data. The differing peak heights (especially the third peak) between the models are clear (though not large) and the data therefore offer an additional constraint that slightly alters the observed degeneracy. The bottom panel of Fig. 5 shows three models that lie along the observed degeneracy, again with $\Omega_m = 0.93, 0.36, 0.11$. The narrow angle of

intersection between contours of constant $\Omega_m h^{3.4}$ and $\Omega_m h^2$ [only $10°$ in the $(\ln \Omega_m, \ln h)$ plane] explains why the likelihood banana is long.

The exponent of h for constant θ_H varies slowly from 2.9 to 4.1 as ω_m varies from 0.06 to 0.26. Note that Hu et al. (2001) quote an exponent of 3.8 for constant ℓ_1; the difference from 3.4 is mainly caused by the slight dependence of ϕ_1 on ω_m, which we ignored above. However, since that paper, improved CMB data has better revealed the second and third peaks, and the exponent of 3.4 is more appropriate for preserving the mean location of the first three peaks. Also, note that the near-integer exponent of 3.0 for the likelihood ridge in Fig. 4 is a coincidence that depends on the observed value of ω_m, details of the CMB error bars, etc. However, the arguments above are fairly generic, so we anticipate that any CMB data set covering the first few peaks should (assuming flatness) give a likelihood ridge elongated along a contour of constant $\Omega_m h^p$, with p fairly close to 3.

To summarize this section, the CMB peak locations are closely related to the angle subtended by the sound horizon at recombination, which we showed is a near-constant fraction of the light horizon angle given in equation (12). We have thus called this the 'horizon angle degeneracy', which has more physical content than the alternative 'peak location degeneracy'. A contour of constant θ_S is very well approximated by a line of constant $\Omega_m h^{3.4}$, and information on the peak heights slightly 'rotates' the measured likelihood ridge near to a contour of constant $\Omega_m h^{3.0}$.

5 CONSTRAINING QUINTESSENCE

There has been recent interest in a possible extension of the standard cosmological model that allows the equation of state of the vacuum energy $w \equiv p_{vac}/\rho_{vac} c^2$ to have $w \neq -1$ (e.g. Zlatev, Wang & Steinhardt 1999), thereby not being a 'cosmological constant', but a dynamically evolving component. In this section we extend our analysis to constrain models with $w \geqslant -1$; we assume w does not vary with time since a model with time-varying w generally looks very similar to a model with a suitably chosen constant w (e.g. Kujat et al. 2002). The shapes of the CMB and matter power spectra are invariant to changes of w (assuming the vacuum energy was negligible before recombination): the only significant effect is to alter the angular diameter distance to last scattering, and move the angles at which the acoustic peaks are seen. For flat models, a useful approximation to the present-day horizon size is given by

$$r_H(z = 0) = \frac{2c}{H_0}\Omega_m^{-\alpha}, \qquad \alpha = \frac{-2w}{1 - 3.8w} \qquad (15)$$

(compare with equation 7 for $w = -1$). As discussed previously, the primary constraint from the CMB data is on the angle subtended today by the light horizon (given for $w = -1$ models by equation 12). If w is increased from -1 at fixed Ω_m, h, the peaks in the CMB angular power spectrum move to larger angles. To continue to fit the CMB data, we must decrease $\Omega_m h^{3.4}$ to bring θ_H back to its 'best-fitting' value. However, the 2dFGRS power spectrum constraint limits $\Omega_m h = 0.20 \pm 0.03$, so to continue to fit both CMB + 2dFGRS we must reduce h.

The CMB and 2dFGRS data sets alone therefore constrain a combination of w and h, but not both separately. The dashed lines in Fig. 6 show likelihood contours for w against h fitting to both the CMB and 2dFGRS power spectra showing this effect. Here, we have marginalized over Ω_m assuming a uniform prior $0.0 < \Omega_m < 1.3$. An extra constraint on h can be converted into a limit on w: if we
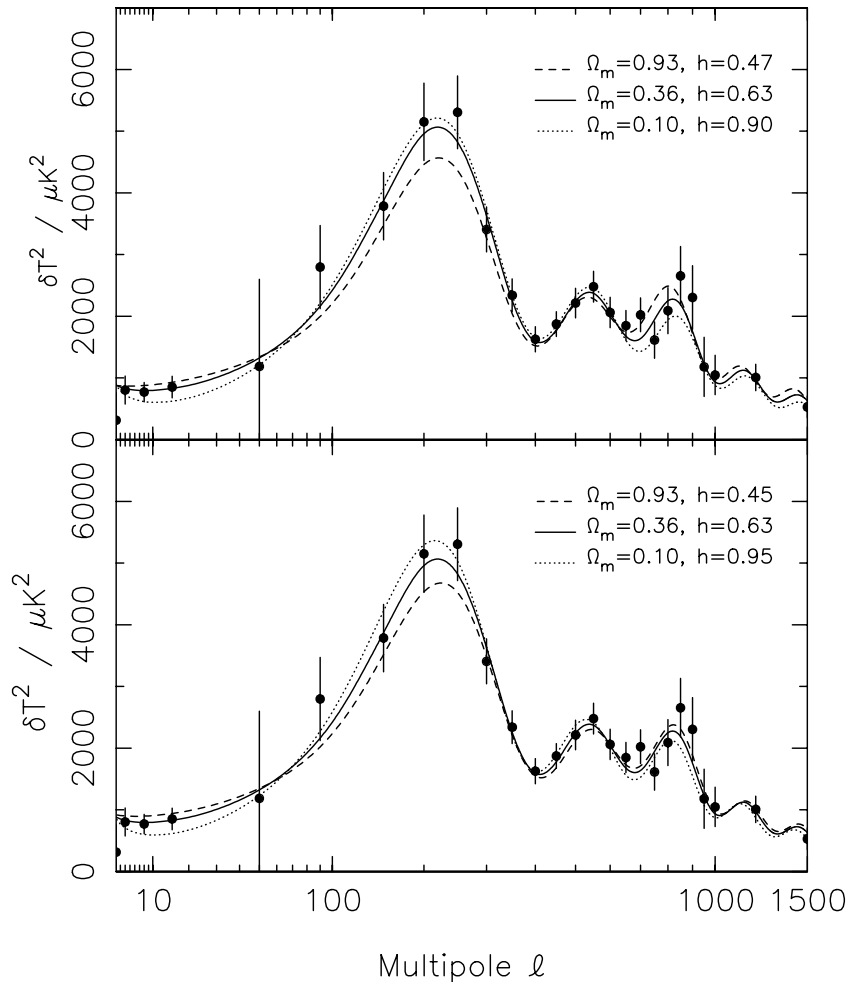
Figure 5. The top panel shows three scalar-only model CMB angular power spectra with the same apparent horizon angle, compared with the data of Table 1. Although these models have approximately the same value of $\Omega_m h^{3.4}$, they are distinguishable by peak heights. Such additional constraints alter the degeneracy observed in Fig. 4 slightly from $\Omega_m h^{3.4}$ to $\Omega_m h^{3.0}$. Three scalar-only models that lie in the likelihood ridge with $\Omega_m h^{3.0}$ are compared with the data in the bottom panel. For all of the models shown, parameters other than Ω_m and h have been adjusted to their maximum-likelihood positions.

include the measurement $h = 0.72 \pm 0.08$ from the *Hubble Space Telescope* (*HST*) key project (Freedman et al. 2001) we obtain the solid likelihood contours in Fig. 6. The combination of these three data sets then gives $w < -0.52$ (95 per cent confidence); the limit of the range considered, $w = -1.0$, provides the smallest uncertainty. The 95 per cent confidence limit is comparable to the $w < -0.55$ obtained from the supernova Hubble diagram plus flatness (Garnavich et al. 1998). See also Efstathiou (1999), who obtained $w < -0.6$ from a semi-independent analysis combining CMB and supernovae (again assuming flatness).

6 PREDICTING THE CMB POWER SPECTRUM

An interesting aspect of this analysis is that the current CMB data are rather inaccurate for $20 \lesssim \ell \lesssim 100$, and yet the allowed CDM models are strongly constrained. We therefore consider how well this model-dependent determination of the CMB power spectrum is defined, in order to see how easily future data could test the basic CDM + flatness paradigm.

Using our grid of $\sim 2 \times 10^8$ models, we have integrated the CMB + 2dFGRS likelihood over the range of parameters presented in Table 3 in order to determine the mean and rms CMB power at

each ℓ. These data are presented in Table 5 at selected ℓ values, and the range of spectra is shown by the grey-shaded region in the top panel of Fig. 7. A possible tensor component was included in this analysis, although this has a relatively minor effect, increasing the errors slightly (as expected when new parameters are introduced), but hardly affecting the mean values. The predictions are remarkably tight: this is partly because combining the peak-location constraint on $\Omega_m h^{3.4}$ with the 2dFGRS constraint on $\Omega_m h$ gives a better constraint on $\Omega_m h^2$ than the CMB data alone, and this helps to constrain the predicted peak heights.

The bottom panel of Fig. 7 shows the errors on an expanded scale, compared with the cosmic variance limit and the predicted errors for the *MAP* experiment (Page 2002). This comparison shows that, while *MAP* will beat our present knowledge of the CMB angular power spectrum for all $\ell \lesssim 800$, this will be particularly apparent around the first peak. As an example of the issues at stake, the scalar-only models predict that the location of the first CMB peak should be at $\ell = 221.8 \pm 2.4$. Significant deviations observed by *MAP* from such predictions will imply that some aspect of this model (or the data used to constrain it) is wrong. Conversely, if the observations of *MAP* are consistent with this band, then this will be strong evidence in favour of the model.

Table 5. The predicted mean and rms CMB power calculated by integrating the CMB + 2dFGRS likelihood over the range of parameters presented in Table 3, allowing for a possible tensor component. These data form a testable prediction of the CDM + flatness paradigm.

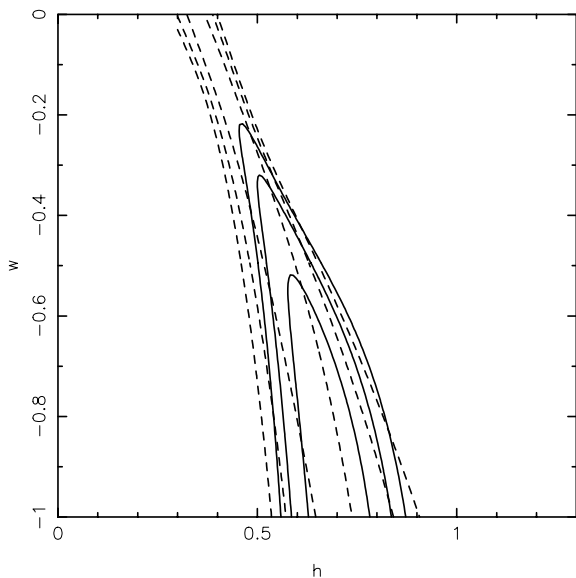| ℓ	δT^2 (μK^2)	rms error (μK^2)
2	920	134
4	817	102
8	775	88
15	828	96
50	1327	100
90	2051	87
150	3657	172
200	4785	186
250	4735	150
300	3608	113
350	2255	82
400	1567	52
450	1728	79
500	2198	86
550	2348	74
600	2052	76
650	1693	51
700	1663	79
750	1987	131
800	2305	122
850	2257	93
900	1816	107
950	1282	93
1000	982	46
1200	1029	69
1500	686	60

Figure 6. Likelihood contours for the equation of state of the vacuum energy parameter w against the Hubble constant h. Dashed contours are for CMB + 2dFGRS data, solid contours include also the *HST* key project constraint. Contours correspond to changes in the likelihood from the maximum of $2\Delta \ln \mathcal{L} = 2.3, 6.0, 9.2$. Formally, this results in a 95 per cent confidence limit of $w < -0.52$.

7 SUMMARY AND DISCUSSION

Following recent releases of CMB angular power spectrum measurements from VSA and CBI, we have produced a new compilation of data that estimates the true power spectrum at a number of nodes, assuming that the power spectrum behaves smoothly between the nodes. The best-fitting values are not convolved with a window function, although they are not independent. The data and Hessian matrix are available from http://www.roe.ac.uk/~wjp/CMB/. We have used these data to constrain a uniform grid of $\sim 2 \times 10^8$ flat cosmological models in seven parameters jointly with 2dFGRS large-scale structure data. By fully marginalizing over the remaining parameters we have obtained constraints on each, for the cases of CMB data alone, and CMB + 2dFGRS data. The primary results of this paper are the resulting parameter constraints, particularly the tight constraints on h and the matter density Ω_m: combining the 2dFGRS power spectrum data of Percival et al. (2001) with the CMB data compilation of Section 2, we find $h = 0.665 \pm 0.047$ and $\Omega_m = 0.313 \pm 0.055$ (standard rms errors), for scalar-only models, or $h = 0.700 \pm 0.053$ and $\Omega_m = 0.275 \pm 0.050$, allowing a possible tensor component.

We have also discussed in detail how these parameter constraints arise. Constraining $\Omega_{tot} = 1$ does not fully break the geometrical degeneracy present when considering models with varying Ω_{tot}, and models with CMB power spectra that peak at the same angular position remain difficult to distinguish using CMB data alone. A simple derivation of this degeneracy was presented, and models with constant peak locations were shown to closely follow lines of constant $\Omega_m h^{3.4}$. We can note a number of interesting phenomenological points from this analysis.

(i) The narrow CMB Ω_m–h likelihood ridge in Fig. 4 derives primarily from the peak locations, therefore it is insensitive to many of the parameters affecting peak heights, e.g. tensors, n_s, τ, calibration uncertainties, etc. Of course it is strongly dependent on the flatness assumption.

(ii) This simple picture is broken in detail as the current CMB data obviously place additional constraints on the peak heights. This changes the degeneracy slightly, leading to a likelihood ridge near constant $\Omega_m h^3$.

(iii) The high power of h^3 means that adding an external h constraint is not very powerful in constraining Ω_m, but an external Ω_m constraint gives strong constraints on h. A 10 per cent measurement of Ω_m (which may be achievable, for example, from evolution of cluster abundances) would give a 4 per cent measurement of h.

(iv) When combined with the 2dF power spectrum shape (which mainly constrains $\Omega_m h$), the CMB + 2dFGRS data gives a constraint on $\Omega_m h^2 = 0.1322 \pm 0.0093$ (including tensors) or $\Omega_m h^2 = 0.1361 \pm 0.0096$ (scalars only), which is considerably tighter from the CMB alone. Subtracting the baryons gives $\Omega_c h^2 = 0.1096 \pm 0.0092$ (including tensors) or $\Omega_c h^2 = 0.1151 \pm 0.0091$ (scalars only), accurate results that may be valuable in constraining the parameter space of particle dark matter models and thus predicting rates for direct-detection experiments.

(v) We can understand the solid contours in Fig. 4 simply as follows: the CMB constraint can be approximated as a one-dimensional stripe $\Omega_m h^{3.0} = 0.0904 \pm 0.0092$ (including tensors) or $\Omega_m h^{3.0} = 0.0876 \pm 0.0085$ (scalars only), and the 2dF constraint as another stripe $\Omega_m h = 0.20 \pm 0.03$. Multiplying two Gaussians with the above parameters gives a result that looks quite similar to the fully marginalized contours. In fact, modelling the CMB constraint simply using the location of the peaks to give $\Omega_m h^{3.4} = 0.081 \pm 0.012$ (including tensors) or $\Omega_m h^{3.4} =$
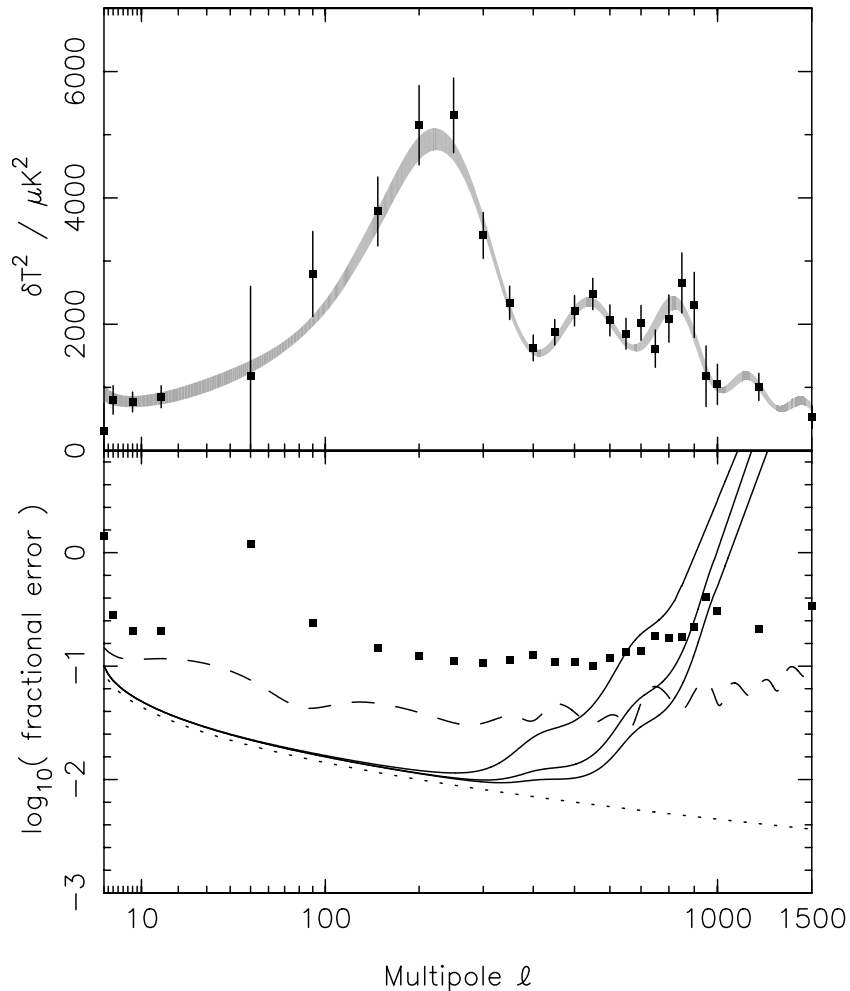
Figure 7. Upper panel: the grey-shaded region shows our prediction of the CMB angular power spectrum with 1σ errors (see the text); points show the data of Table 1. The lower panel shows fractional errors: points are the current data, dashed line is the errors on our prediction, and the three solid lines are expected errors for the *MAP* experiment (Page 2002) for $\Delta\ell = 50$ and the 6-month, 2- and 4-yr data (top to bottom). The dotted line shows the expected cosmic variance, again for $\Delta\ell = 50$, assuming full sky coverage (the *MAP* errors assume 80 per cent coverage). As can be seen, the present CMB and LSS data provide a strong prediction over the full ℓ-range covered by MAP.

0.073 ± 0.010 (scalars only) also produces a similar result, demonstrating that the primary constraint of the CMB data in the $(\Omega_{\rm m}, h)$ plane is on the apparent horizon angle.

In principle, accurate non-CMB measurements of both $\Omega_{\rm m}$ and h can give a robust prediction of the peak locations assuming flatness. If the observed peak locations are significantly different, this would give evidence for either non-zero curvature, quintessence with $w \neq -1$ or some more exotic failure of the model. Using the CMB data to constrain the horizon angle, and 2dFGRS data to constrain $\Omega_{\rm m}h$, there remains a degeneracy between w and h. This can be broken by an additional constraint on h; using $h = 0.72 \pm 0.08$ from the *HST* key project (Freedman et al. 2001), we find $w < -0.52$ at 95 per cent confidence. This result is comparable to that found by Efstathiou (1999) who combined the supernovae sample of Perlmutter et al. (1999) with CMB data to find $w < -0.6$.

In Section 6 we considered the constraints that combining the CMB and 2dFGRS data place on the CMB angular power spectrum. This was compared with the predicted errors from the *MAP* satellite in order to determine where *MAP* will improve on the present data and provide the strongest constraints on the cosmological model.

It will be fascinating to see whether *MAP* rejects these predictions, thus requiring a more complex cosmological model than the simplest flat CDM-dominated universe.

Finally, we announce the public release of the 2dFGRS power spectrum data and associated covariance matrix determined by Percival et al. (2001). We also provide code for the numerical calculation of the convolved power spectrum and a window matrix for the fast calculation of the convolved power spectrum at the data values. The data are available from either http://www.roe.ac.uk/~wjp/ or from http://www.mso.anu.edu.au/2dFGRS; as we have demonstrated, they are a critical resource for constraining cosmological models.

REFERENCES

Ahmad Q. et al., 2002, Phys. Rev. Lett., 89, 011301
Bond J.R., Efstathiou G., Tegmark M., 1997, MNRAS, 291, L33
Bond J.R., Jaffe A.H., Knox L., 2000, ApJ, 533, 19
Bond J.R. et al., 2002, ApJ, submitted (astro-ph/0205386)
Colless M. et al., 2001, MNRAS, 328, 1039
Doran M., Lilley M., 2002, MNRAS, 330, 965
Efstathiou G., 1999, MNRAS, 310, 842
Efstathiou G., 2002, MNRAS, 332, 193
Efstathiou G., Bond J.R., 1999, MNRAS, 304, 75
Efstathiou G., Sutherland W., Maddox S., 1990, Nat, 348, 705
Efstathiou G. et al., 2002, MNRAS, 330, 29
Eisenstein D.J., Hu W., 1998, ApJ, 496, 605
Elgaroy O. et al., 2002, Phys. Rev. Lett., 89, 061301
Freedman W.L. et al., 2001, ApJ, 553, 47
Garnavich P.M. et al., 1998, ApJ, 509, 74
Halverson N.W. et al., 2002, ApJ, 568, 38
Hu W., Sugiyama N., 1995, ApJ, 444, 489
Hu W., Fukugita M., Zaldarriaga M., Tegmark M., 2001, ApJ, 549, 669
Knox L., Christensen N., Skordis C., 2001, ApJ, 563, L95
Kolb E.W., Turner M.S., 1990, The Early Universe. Addison-Wesley, Reading, MA
Kujat J., Linn A.M., Scherrer R.J., Weinberg D.H., 2002, ApJ, 572, 1
Lahav O. et al., 2002, MNRAS, 333, 961
Lee A.T. et al., 2001, ApJ, 561, L1

Lewis A., Bridle S., 2002, Phys. Rev. D submitted (astro-ph/0205436)
Liddle A.R., Lyth D.H., 2000, Cosmological Inflation and Large-Scale Structure. Cambridge Univ. Press, Cambridge
Loeb A., Barkana R., 2001, ARAA, 39, 19
Mason B.S. et al., 2002, ApJ, submitted (astro-ph/0205384)
Netterfield C.B. et al., 2002, ApJ, 571, 604
Page L., 2002, in Sato K., Shiromizu T., eds, New Trends in Theoretical and Observational Cosmology. Universal Academy Press, Tokyo (astro-ph/0202145)
Peacock J.A. et al., 2001, Nat, 410, 169
Pearson T.J. et al., 2002, ApJ, submitted (astro-ph/0205388)
Peebles P.J.E., 1984, ApJ, 284, 444
Percival W.J. et al., 2001, MNRAS, 327, 1297
Perlmutter S. et al., 1999, ApJ, 517, 565
Press W.H., Teukolsky S.A., Vetterling W.T., Flannery B.P., 1992, Numerical Recipes in C, 2nd edn. Cambridge Univ. Press, Cambridge
Scott P.F. et al., 2002, MNRAS, submitted (astro-ph/0205380)
Seljak U., Zaldarriaga M., 1996, ApJ, 469, 437
Tegmark M., 1996, ApJ, 464, L35
Vittorio N., Silk J., 1985, ApJ, 297, L1
Wang X., Tegmark M., Zaldarriaga M., 2002, Phys. Rev. D, 65, 123001
Zaldarriaga M., Spergel D.N., Seljak U., 1997, ApJ, 488, 1
Zlatev I., Wang L., Steinhardt P.J., 1999, Phys. Rev. Lett., 82, 896

This paper has been typeset from a TEX/LATEX file prepared by the author.